Comparing the Dual-Mode VCSEL in OM4-MMF and GI-SMF Links for NRZ-OOK and 16-QAM-OFDM Transmissions

Shao-Yung Lee, Chih-Hsien Cheng, *Member, IEEE*, Hsien-Yao Tseng, Xin Chen, Wei-Chi Lo, Kangmei Li, Chia-Hsuan Wang, Cheng-Ting Tsai, Hao-Chung Kuo, *Fellow, IEEE*, Ming-Jun Li, *Fellow, IEEE*, and Gong-Ru Lin, *Fellow, IEEE*

***Abstract*—A dual-mode (DM) vertical-cavity surface-emitting laser (VCSEL) is investigated for carrying high-speed data transmission with either the non-return-zero on-off keying (NRZ-OOK) or the quadrature amplitude modulation-orthogonal frequency division multiplexing (QAM-OFDM) format. In both the back-to-back (BtB) and the 100-m transmission cases with using either the OM4 multimode fiber (OM4-MMF) or the graded-index single-mode fiber (GI-SMF), the mismatch between the core diameter of the lensed MMF pick-up head and the mode field of the DM-VCSEL output controls the coupled transverse mode number and decrease the modal dispersion effect. Using pre-emphasized NRZ-OOK data can compensate the SNR degradation to improve the BER to 5.6×10^{-12} under BtB and 6.9×10^{-10} after 100-m GI-SMF for the DM-VCSEL delivered NRZ-OOK data at 53 Gbit/s. For 16-QAM OFDM transmission, the pre-leveling algorithm shows better data compensation than the pre-emphasis algorithm in both BtB and the 100-m GI-SMF cases. With the pre-leveling compensation of the 16-QAM OFDM data encoded to the DM-VCSEL with a 0.4-dB/GHz slope, the DM-VCSEL allows 136 Gbit/s for BtB, 112 Gbit/s for 100-m OM4-MMF, and 92 Gbit/s for 100-m GI-SMF transmissions. The pre-emphasis NRZ-OOK and the pre-leveling 16-QAM OFDM data carried by the DM-VCSEL can be used in ultrahigh-speed intra-data-center links in the future.**

***Index Terms*—Dual-mode vertical-cavity surface-emitting laser, graded-index single-mode fiber (GI-SMF), NRZ-OOK, QAM-OFDM.**

Manuscript received January 27, 2022; revised March 25, 2022; accepted April 12, 2022. Date of publication April 19, 2022; date of current version May 5, 2022. This work was supported by the Ministry of Science and Technology, Taiwan under Grants MOST 109-2221-E-002-184-MY3, MOST 110-2221-E-002-100-MY3, MOST 110-2124-M-A49-003-, MOST 110-2224-E-992-001-, and MOST 111-2119-M-002-009-. *(Shao-Yung Lee and Chih-Hsien Cheng are co-first authors.) (Corresponding authors: Gong-Ru Lin; Hao-Chung Kuo.)*

Shao-Yung Lee, Wei-Chi Lo, Cheng-Ting Tsai, and Gong-Ru Lin are with the Graduate Institute of Photonics and Optoelectronics and the Department of Electrical Engineering, National Taiwan University, Taipei 10617, Taiwan (e-mail: grlin@ntu.edu.tw).

Chih-Hsien Cheng is with the Research Center for Advanced Science and Technology, University of Tokyo, Tokyo 153-0041, Japan.

Hsien-Yao Tseng is with the Department of Photonics and Institute of Electro-optic Engineering, National Yang-Ming Chiao-Tung University, Hsinchu 30010, Taiwan.

Xin Chen, Kangmei Li, Chia-Hsuan Wang, and Ming-Jun Li are with the Corning Inc., Corning, NY 14831 USA.

Hao-Chung Kuo is with the Department of Photonics and Institute of Electro-optic Engineering, National Yang-Ming Chiao-Tung University, Hsinchu 30010, Taiwan, and also with Semiconductor Research Center, Hon Hai Research Institute, Taipei 11492, Taiwan (e-mail: hckuo@faculty.nctu.edu.tw).

Digital Object Identifier 10.1109/JPHOT.2022.3168626

I. Introduction

In RECENT years, the demand for high-resolution media, data stream, and data cloud storage/computing has become a key driver for the rapid development of high-speed data transmission. In the IEEE P802.3bs standard [1], the transmission speed is increased from 100 Gbit/s to 400 Gbit/s for future intra-data-center applications. In the early stage, the transmission structure can be based on an 8-channel vertical-cavity surface-emitting laser (VCSEL) array carrying 50 Gbit/s non-return-to-zero on-off keying (NRZ-OOK) data for each channel [2]. Nowadays, the combination of 850-nm multimode (MM) VCSELs and multimode fibers (MMF) is regarded as one of the best cost-effective solutions to construct intra-data-center links [3]–[8]. The MM VCSEL + MMF link offers advantages of efficient laser to fiber coupling and low power consumption due to the low threshold and high-power conversion efficiency in the MM VCSEL [9], [10]. These advantages make the MM VCSEL the best candidate for intra-data-center applications. However, the modal dispersion in the MMF transmission limits the data rate and the distance [11]. Moreover, the low modulation bandwidth of the MM VCSEL is also an important issue to limit the data rate. To solve these problems, few-mode (FM) or single-mode (SM) VCSELs are used to enhance the modulation bandwidth [12]–[14]. Minimizing the diameter of the oxide-confined aperture can increase the transverse mode spacing and reduce the optical field area of the VCSEL. This is critical to control the lasing of the high-order modes for demonstrating the FM or SM lasing in the VCSEL [15]. However, reducing the diameter of the oxide-confined aperture increases the differential resistance of the SM VCSEL, which induces a large signal reflection to degrade the modulation depth [16]. Fortunately, diffusing the heavy zinc (Zn) dopants into the top distributed Bragg reflector (DBR) mirror can achieve better ohmic contact and avoid free-carrier absorption [17]–[19]. A thick benzocyclobutene (BCB) passivation layer with low capacitance can also improve the RC charging/discharging time of the VCSEL [20]. In addition to the VCSEL developments, standard or graded-index single-mode fiber (SMF) links are also utilized to decrease the modal dispersion during the transmission [21]. Besides the transmission system improvement, different data formats have been utilized to enhance the data rate for future intra-data-center

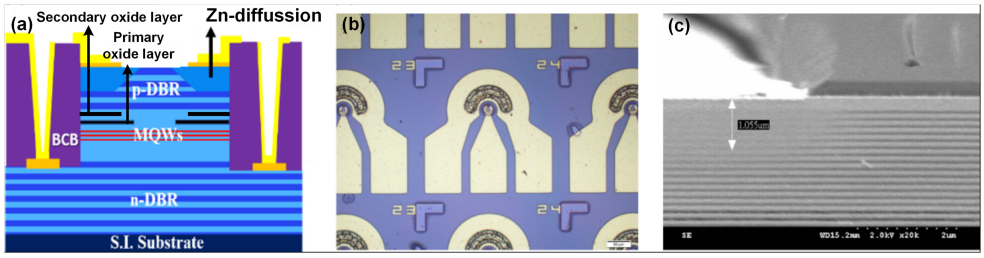

Fig. 1. (a) Layer structure and (b) OM image of the DM-VCSEL. (c) SEM image of Zn-diffusion region in the DM-VCSEL.

applications in recent years. In general, the reported spectral usage efficiency for the NRZ-OOK is low [22]. Hence, the method to enhance the transmission rate for the NRZ-OOK data format only increases the modulation bandwidth of transmission system.

To solve this problem, the PAM-4 data format is used to encode onto the VCSEL because the data rate of the PAM-4 signal can be doubled compared to that of the NRZ-OOK [23]. Moreover, the quadrature amplitude modulation orthogonal frequency division multiplexing (QAM-OFDM) format provides the best spectral usage efficiency compared to the other formats. It improves the data rate under the same modulation bandwidth [24]–[27].

Nevertheless, further reducing the mode number of the VCSEL results in small lasing power, which practically limits its transmission capability in data-center applications. Especially, the decreased emission aperture size via thin-film oxidation and the resistance reduction via high metallic ion doping are hard to be controlled precisely in the fabrication process. The lensed OM4-MMF and GI-SMF coupling links are introduced to control the number of the transverse modes in VCSEL and the modal dispersion during the GI-SMF transmission. In this work, both NRZ-OOK and 16-QAM OFDM formats are encoded to a dual-mode (DM) 850-nm VCSEL. The transmissions in different configurations coupled with lensed OM4-MMF and GI-SMF pick-up heads, linked with 100-m-long OM4-MMF and GI-SMF segments, and optimized with different data compensation algorithms are demonstrated for intra-data-center applications. The fundamental characteristics of the DM-VCSEL such as the power-to-current-voltage (L-I-V) curve, differential resistance, small-signal analog modulation response, relative intensity noise (RIN), and mode partition noise (MPN) are analyzed. The transmission performances of both NRZ-OOK and the 16-QAM OFDM formats in the back-to-back (BtB) and 100-m GI-SMF links are also presented. The key parameters of transmission performance such as signal-to-noise ratio (SNR) and bit error rate (BER) are determined and optimized by different data compensation methods.

II. Experimental Setup

A. Design of the DM -VCSEL Design With 5 μm Aperture

Fig. 1(a) and (b) respectively exhibit the layer structure and an optical microscopic image of the DM-VCSEL. In addition, Fig. 1(c) shows an SEM image of the Zn-diffusion region in the DM-VCSEL. The active design of the VCSEL was composed of 5-pairs of 4.5-nm $In_{0.08}Ga_{0.92}As$ quantum wells (QWs) and 6-pairs of 6-nm $As_{0.37}Ga_{0.63}Al$ quantum barriers. Moreover, the active region was sandwiched between 31-pairs of n-type $Al_{0.12}Ga_{0.88}As/Al_{0.9}Ga_{0.1}As$ DBR and 19-pairs of p-type $Al_{0.12}Ga_{0.88}As/Al_{0.9}Ga_{0.1}As$ DBR layers. These p- and n-type DBR layers were designed to form the cavity of the DM-VCSEL. In the design of the oxide layer, 2-pairs of 55-nm primary oxide layers and 4-pairs of 52-nm secondary oxide layers were utilized to confine the lasing modes of the DM-VCSEL. In this study, the DM-VCSEL exhibits the following characteristics. The gallium arsenide substrate exhibits the semi-insulating property to decrease the VCSEL capacitance.

To enhance the optical confinement factor, the cavity length is set as λ/2. In general, the confinement factor (Γ_z) can be presented as [28],

$$\Gamma_z = (\Gamma_{fill})(\Gamma_{enh}) = \left(\frac{L_a}{L}\right)\left(1 + \frac{\sin \beta L_a}{\beta L_a}\right), \quad (1)$$

where $\beta = 2\pi\bar{n}/\lambda$ is the propagation constant in the active region with $\bar{n}$ and λ denoting the effective refractive index and the wavelength, L_a is the sum of the cavity length and the phase penetration lengths of the distributed Bragg reflectors, L is the thickness of the active layer, Γ_{fill} and Γ_{enh} are the respective filling factor and enhance factor. The cavity length was shortened to λ/2 not only for reducing the internal carrier transient time but also for increasing the optical confinement factor, as the L_a/L term must be increased as high as possible and the active region must be placed in the antinode of the standing wave to enhance the confinement factor. In addition, the multiple pairs of oxide layers are also used to decrease the VCSEL capacitance. The strained QW is utilized to enlarge the differential gain in the DM-VCSEL. For the parasitic effect, the low dielectric constant in the BCB insulating material decreases the electrode capacitance. To further reduce the parasitic resistance, the doping concentrations of DBRs are decreased and designed into a gradual distribution for decreasing the energy band difference in the heterojunction. The DM-VCSEL wafer was provided by a commercial manufacturer. The fabrication processes of the DM-VCSEL include photolithography, inductively coupled plasma reactive ion etching (ICP-RIE) mesa etch, Zn-diffusion, wet oxidation, passivation, metallization, planarization, etc. First, the zinc diffusion process was used to form the Zn-diffusion window with a diameter of 4 μm and a depth of 1 μm. The p-type ring Ti/Pt/Au metal contact was deposited. The DM-VCSEL wafer was etched 4 μm to n-type DBR layer via the ICP-RIE process. The wafer was sent to the furnace tube for performing wet oxidation. Afterward, the ring-shaped n-type Au/Ge/Ni/Au metal contact was deposited. The post-annealing method was utilized to form ohmic contacts.

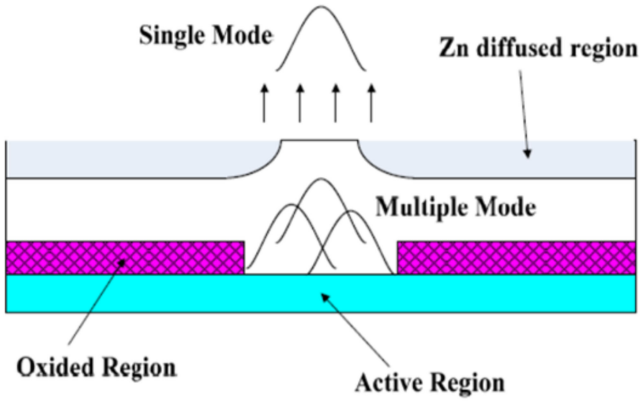

Fig. 2. Schematic diagram of the mode selection by the Zn-diffusion on the p-DBR layer.

The BCB layer was employed for the planarization process. At last, the photolithography formed the contact holes of both p- and n-type layers. Finally, a coplanar RF electrode (Ti/Au) was deposited.

B. Principle of the GI-SMF

In this work, the Zn-diffusion method is used to decrease the transverse mode of the VCSEL. The Zn-diffusion in the p-DBR will result in impurity-induced disordering [29] to change the effective energy gap and refractive index in the desired regions of the hetero-structures. The impurity-induced disordered DBR region exhibits an Al composition that is the average of the original $Al_xGa_{1-x}As$ layers with high and low Al contents due to the greatly increased self-diffusion of Al and Ga. The p-type Zn dopant reveals a uniformly diffused concentration in the disordered region in the $Al_xGa_{1-x}As$ layer [30], which is employed to create a selective gain-loss mechanism for higher-order modes in the peripheral region of the top DBR of the VCSEL, as shown in Fig. 2.

To further suppress the transverse modes of the VCSEL during the transmission, a novel GI-SMF is used for VCSEL transmission [21]. The refractive index profile of the GI-SMF can be described by

$$n(r) = n_0 \cdot \sqrt{1 - 2\Delta(r/a)^{\alpha}}, \tag{2}$$

where n_0 is the refractive index in the center of the fiber core, a denotes the fiber core radius, $\Delta = (n_0^2\text{-}n_1^2)/(2n_0^2)$ the relative index difference between the core center and the cladding with n_1 denoting the refractive index of the cladding. The profile of the refractive index is dependent on the parameter (α).

By setting the parameters of the fiber core and cladding, a graded-index fiber can exhibit the mode field diameter, cable cutoff wavelength, zero-dispersion wavelength, and other properties to meet the requirements of the ITU-T G.652 standard. This GI-SMF can maintain the standard single-mode operation at both the 1310-nm and the 1550-nm wavelength windows. In addition, this GI-SMF also supports the LP_{01} and LP_{11} modes in the wavelength window around 850 nm. The modal bandwidth at 850 nm can be maximized for few-mode VCSEL-based

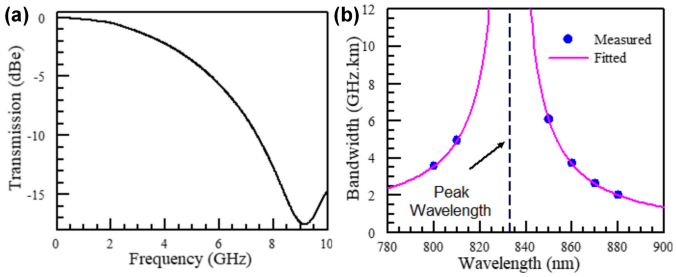

Fig. 3. (a) Transfer function of 1-km GI-SMF at 850 nm. (b) Measured and fitted modal bandwidths of the GI-SMF at different wavelengths.

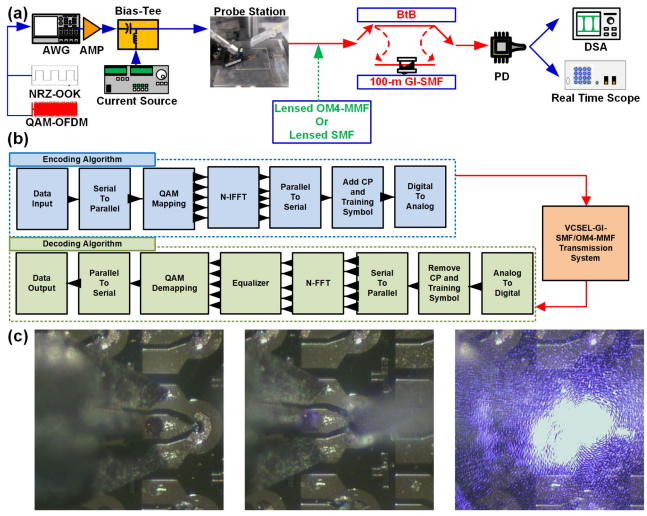

Fig. 4. (a) Measuring system for testing the transmission performance of the DM-VCSEL. (b) The block diagrams of the QAM OFDM data algorithm processing. (c) Microscopic diagram and light emission of the DM-VCSEL.

transmission by selecting the appropriate α value. The measured transfer function and modal bandwidths at different wavelengths for the1 km GI-SMF are shown in Fig. 3. For this fiber, the α value is selected around 2.5 to maximize the bandwidth at 850 nm in previous works [21], [31].

C. Measuring System for Testing the Transmission Performance of the DM-VCSEL

The measuring system for testing the transmission performance of the DM-VCSEL is shown in Fig. 4(a). The QAM-OFDM data was generated by a MATLAB program and sent to an arbitrary waveform generator (AWG, Keysight M8194A). Fig. 4(b) shows the flow chart of the QAM-OFDM data algorithm processing. In this work, pseudorandom binary sequence (PRBS) data of the NRZ-OOK format with a length of 2^{15}-1 was serial-to-parallel mapped onto 16-QAM symbols. Then, the inverse fast Fourier transform (IFFT) with an FFT size of 512 was utilized to convert the OFDM subcarriers into a time-domain waveform. In addition, the cyclic prefix (CP) with a ratio of 1/32 and a training symbol (TS) with a ratio of 1/32 were inserted into the time-domain OFDM waveform to avoid inter-symbol interference (ISI) after the GI-SMF/OM4-MMF transmission.

After digital-to-analog conversion, the converted data was injected into DM-VCSEL to perform the GI-SMF/OM4-MMF transmission. After the GI-SMF/OM4-MMF transmission, the received data was analog-to-digital converted to perform the demodulation. After removing the CP and TS, the time-domain OFDM waveform was converted to OFDM subcarriers by FFT and equalizer methods. After the QAM demapping and the parallel-to-serial conversion, the received PRBS data can be obtained. The electrical NRZ-OOK and QAM-OFDM data streams were generated from an AWG with a sampling rate of 120 GSa/s. The peak-to-peak amplitude (V_{pp}) of the electrical NRZ-OOK and QAM-OFDM signals were amplified via a microwave amplifier (Anritsu AH54147A). Then, the NRZ-OOK/QAM-OFDM data and DC bias current were combined within a bias-tee (Anritsu V250) to drive the DM-VSCEL by a ground-signal-ground (GSG) microwave probe. The output power of the DM-VCSEL was collected by a lensed OM4-MMF and lensed SMF with respective core diameters of 50 μm and 9 μm. The coupling performance was analyzed at several different tilting angles away from the surface normal of the DM-VCSEL. For 100-m GI-SMF transmission, the output from the lensed OM4-MMF/lensed SMF was directly coupled into the GI-SMF with a core diameter of 12 μm. In the BtB and 100-m GI-SMF conditions, the transmitted data from the DM-VCSEL was received via a photoreceiver (Newport 1484-A-50) to perform the optical-to-electrical conversion. For analyzing the transmission performance of different data formats, the received NRZ-OOK data was captured by a digital serial analyzer (DSA, Tektronix 8300). The received QAM-OFDM data was caught via a real-time scope (Tektronix DPO77002SX). To improve the received SNR and BER, the waveform pre-emphasis method was utilized to perform the signal compensation including amplitude and phase for achieving the maximal data rates of the NRZ-OOK/QAM-OFDM formats.

Fig. 4(c) shows the microscopic diagram and light emission of the DM-VCSEL. The left part of Fig. 4(c) shows the microscopic images of the microwave probe connecting with the DM-VCSEL in the left insight, the lensed fiber head moving to the top of the DM-VCSEL in the middle insight, and the emitted light of the DM-VCSEL coupled by the lensed fiber head in the right insight of Fig. 4(c). A microwave probe was used to supply the bias current and data into the DM-VCSEL. The modulated optical signals from the DM-VCSEL were coupled to the GI-SMF through the lensed MMF/SFM for transmission testing.

III. Result and Discussion

A. The Basic Characteristic of the DM-VCSEL

In this experiment, different types of fiber coupling methods are used. The related P-I curves, the coupling ratio, and the optical spectra for different fiber coupling methods are shown in Fig. 5(a)–(d). In the BtB condition, the optical spectrum of the DM-VCSEL received by the lensed MMF exhibits two obvious peaks at 852.92 and 850.72 nm with respective powers of -4.73 dBm and -10.37 dBm. In addition, some small peaks are also observed around 847.78 to 848.59 nm with corresponding powers lower than -44.92 dBm. Moreover, the total power of the DM-VCSEL received by the lensed MMF is measured as 2.2 mW. When the fiber coupling method changes from the lensed MMF to the lensed SMF, the P-I curve of the DM-VCSEL received by the lensed SMF shows almost a similar trend as that by the OM4-MMF. However, a lower coupling ratio of 9.9% for the lensed SMF coupling reduces the receiving output power to 0.21 mW and makes the small emitted peaks at the same positions disappear. For the 100-m GI-SMF transmission, the core diameter mismatch between the lensed MMF and GI-SMF results in low coupling efficiency of 26.1%, which corresponds to an output power of 0.55 mW after the GI-SMF coupling.

The peak powers of the two main emitted peaks at 852.92 nm and 850.72 nm are decreased to -13.21 dBm and -14.49 dBm, respectively. In addition, the other smaller emitted peaks are hard to observe because of the low coupling ratio between the lensed MMF and GI-SMF. For the fiber coupling between the lensed SMF and GI-SMF, the similar core diameters between both fibers induce a small coupling loss to obtain an output power of 0.18 mW. The coupling loss between the lensed OM4-MMF and GI-SMF is 74%, much higher than that between the lensed SMF and GI-SMF of 15%. However, the received output power collected by the lensed OM4-MMF is much higher than that by the lensed SMF at the beginning. Even though the coupling loss between the lensed MMF and GI-SMF is high, the final output power for the lensed MMF/GI-SMF case is still higher than the SMF/GI-SMF case. Despite the low coupling efficiency due to the field mismatch between the MMF and GI-SMF, the number of VCSEL modes is reduced, which may be an advantage for transmission. In our measurement, the DM-VCSEL maintains its dual transverse modes remains under the bias ranged between 2 mA and 8 mA, as shown in Fig. 6.

The P-I curve of the DM-VCSEL received by the lensed MMF is shown in Fig. 7(a). The DM-VCSEL exhibits a threshold current of 1.4 mA and maximal output power of 2.2 mW before the power saturation. In addition, the power-to-current slope (dP/dI) in the range between 1.5 mA and 6 mA is determined to be 0.34 W/A above the lasing threshold. This uniform dP/dI curve with small variation can be observed at the bias current between 1.4 mA and 6 mA. Enlarging the bias current of the DM-VCSEL from 6 mA to 8 mA increases the optical power by only 0.8 mW but slightly decreases the dP/dI slope because of the power saturation. This phenomenon can reduce the modulation throughput during transmission. The decreased output power in the P-I curve is observed as the bias current of the DM-VCSEL is further increased to 9 mA. This phenomenon is originated from the Auger effect that increases the non-radiative scattering and reduces the radiative emission quantum efficiency. The saturation in the P-I curve is observed as the bias current of the DM-VCSEL is further increased to 9 mA and beyond. Such a thermal rollover point occurs when the internal optical loss and carrier leakage is predominated by the thermal effect in the core region [32]. In addition, the modulation reflection caused by the impedance matching is also an important issue. The differential resistance of the DM-VCSEL operated at a bias current of 8 mA is 141 Ω, as shown in Fig. 7(b). For commercial microwave instruments, the impedance is usually set at 50 Ω. The impedance mismatch is liked to the reflection coefficient (Γ), the return loss

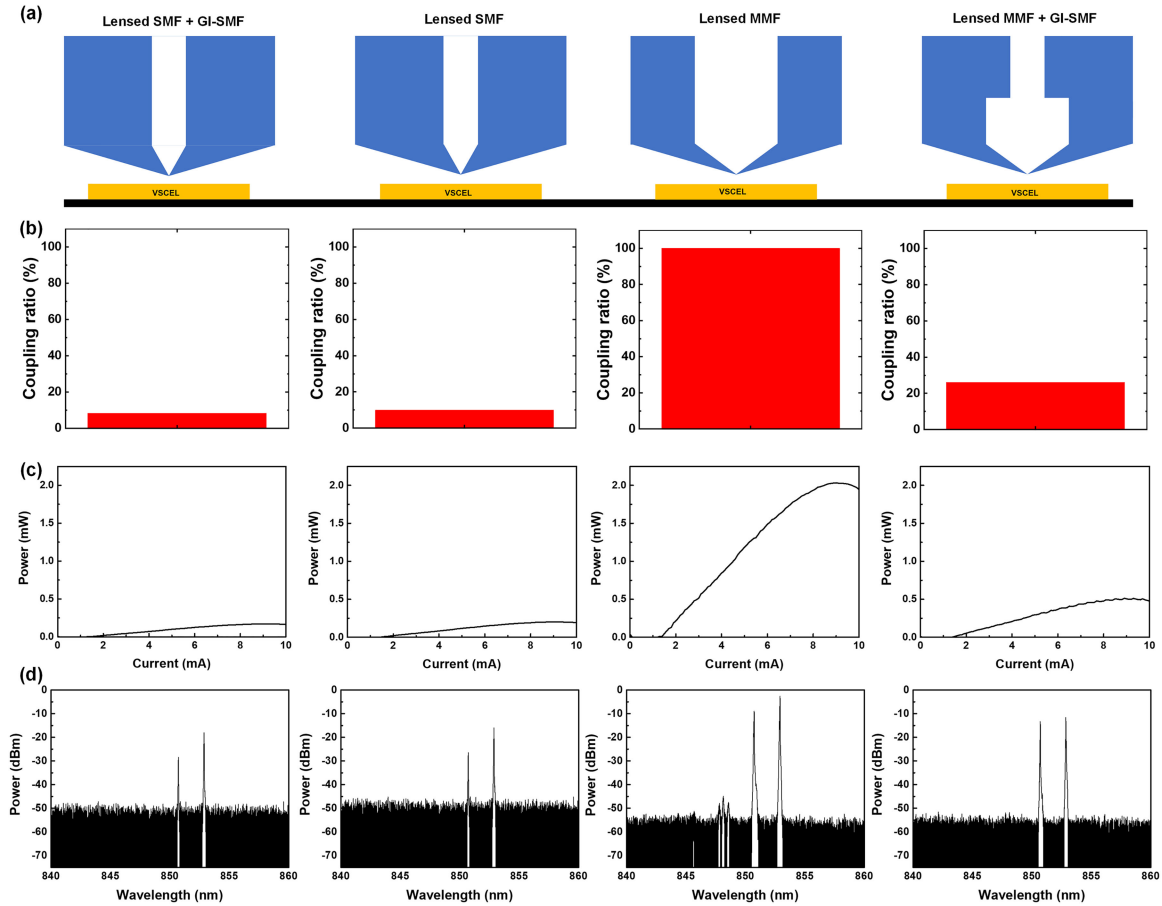

Fig. 5. (a) Coupling schemes and (b) coupling ratios of different fiber coupling methods. (c) P-I responses and (d) optical spectra of the DM-VCSEL received by the different fiber coupling methods.

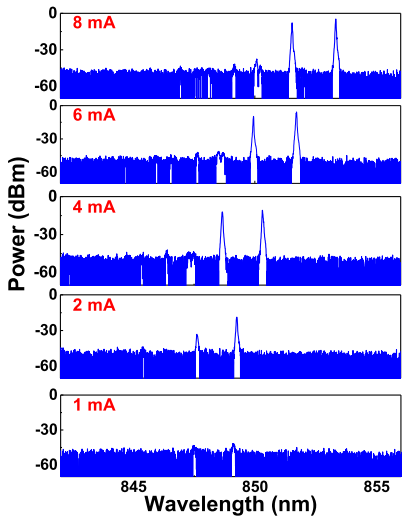

Fig. 6. Optical spectra of the DM-VCSEL under different bias operations.

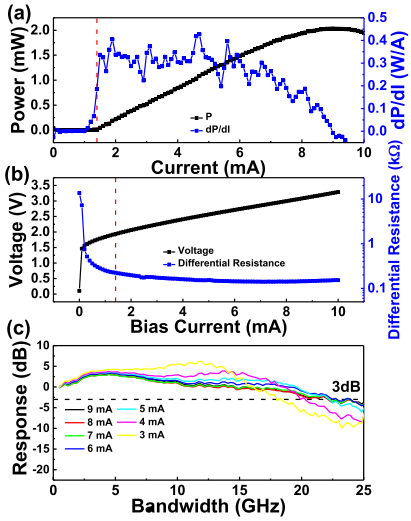

Fig. 7. The (a) P-V curve and dP/dI slope, (b) I-V curve and differential resistance, and (c) frequency response of the DM-VCSEL operated at different bias currents.

(R_L), and the voltage standing wave ratio (VSWR) as follows

$$\begin{cases} \Gamma = \frac{Z_{VCSEL} - Z_{RF}}{Z_{VCSEL} + Z_{RF}} \\ R_L = -20Log\,|\Gamma| \\ VSWR = \frac{1+\Gamma}{1-\Gamma} \end{cases}, \tag{3}$$

where Z_{VCSEL} and Z_{RF} denote the impedances of the VCSEL and the commercial microwave instrument, respectively.

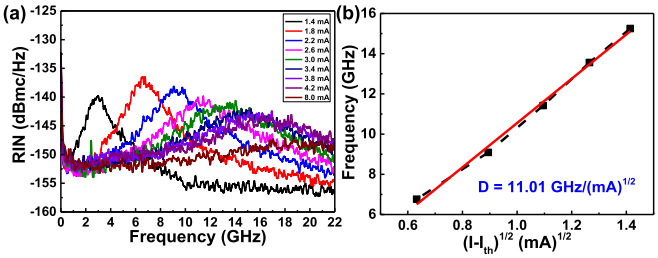

Fig. 8. The (a) RIN spectrum and (b) resonance frequency of the DM-VCSEL operated at different bias currents.

From Eq. (3), the reflection coefficient, the return loss, and the VSWR can be obtained as 0.47, 6.55 dB, and 2.77, respectively, when the DM-VCSEL is operated at the optimized bias current of 8 mA. The frequency responses of the DM-VCSEL operated at different bias currents are also shown in Fig. 7(c). As the bias current increases from 2 mA to 8 mA, the 3-dB bandwidth of the DM-VCSEL improves from 18.3 GHz to 23.1 GHz. However, the 3-dB bandwidth decreases to 22.1 GHz when the bias current further increases to 9 mA. Therefore, the optimized bias current is selected as 8 mA to perform the NRZ-OOK and QAM-OFDM transmission. The noise figure in the RIN spectrum of the VCSEL is another important parameter that degrades the SNR of the data directly carried by the VCSEL. In addition, the broadband noise peak observed in the RIN spectrum is correlated with the relaxation oscillation of the VCSEL. From the RIN spectrum shown in Fig. 8(a), the RIN peak is upshifted from 8 GHz to 21 GHz with the peak power reduced from −135.6 dBc/Hz to −147.5 dBc/Hz by increasing the bias current from 2 mA to 8 mA. Obviously, the relaxation oscillation peak is upshifted to the high frequency. Its power is gradually reduced as the bias current increases [33], [34]. This phenomenon can effectively suppress the noise, which is beneficial for transmission. The resonance frequency distribution of the DM-VCSEL is shown in Fig. 8(b). From Fig. 8(b), the slope known as the D-factor is obtained as 11.01 GHz/mA$^{1/2}$. The D-factor is an important parameter related to the internal quantum efficiency and the differential gain of the quantum wells for the VCSEL. Moreover, the D-factor can be defined as the following formula,

$$f_r = D \times \sqrt{I - I_{th}}, D = \frac{1}{2\pi} \times \sqrt{\frac{\eta_i \Gamma v_g}{qV_a} \times \frac{\partial g}{\partial n}}, \quad (4)$$

where f_r, I, I_{th}, η_i, and Γ denote the resonance frequency, the bias current, the threshold current, the internal quantum efficiency, and the optical confinement factor, respectively. In addition, v_g, q, V_a, and $\partial g/\partial n$ are the group velocity, the elementary charge, the volume of the active (gain) region, and the differential gain, respectively. In principle, the D-factor is dependent on the aperture size of the VCSEL. The smaller aperture size causes the higher photon density to increase the D-factor and resonance frequency.

The dynamic performance of the photon carrier interactions for the VCSEL operated beyond the threshold current can be represented by two equations. One equation is related to the carrier density in the active region and another to the photon density of the lasing mode in the cavity, which are described by

$$\frac{dN}{dt} = \frac{\eta_i I}{qV_a} - \left(AN + BN^2 + CN^3\right) - v_g GS, \quad (5)$$

$$\frac{dS}{dt} = \Gamma v_g GS - \frac{S}{\tau_p} + \Gamma \beta BN^2, \quad (6)$$

where N, G, S, τ_p, and β denote the excess carrier density in the active region, the material gain, the photon density of the lasing mode, the photon lifetime, and the fraction of photons generated by spontaneous emission to go into the lasing mode, respectively.

In addition, the formula of $AN+BN^2+CN^3$ indicates the recombination rate from the spontaneous and non-radiative recombinations, where A, B, and C denote the Shockley-Read-Hall recombination coefficient, the spontaneous emission coefficient, and the Auger recombination coefficient, respectively. By substituting some of the terms in the coupled rate equations and using the first-order Taylor expansion, the small-signal response can be obtained from Eqs. (5) and (6). The replacing terms are set as $I = I_b+\delta I$, $N = N_b+\delta N$, $S = S_b+\delta S$, and $G = g_b/(1+\varepsilon S)+g_0\delta N/(1+\varepsilon S)$ where ε, g_b, and g_0 respectively denote the gain compression factor, the threshold gain due to gain clamping above the threshold, and the nominal differential gain. In addition, the subscript b in I_b, N_b, and S_b indicates the expansion around a biasing point I_b above the threshold. By setting the time derivatives of the steady-state quantities to zero, the equations of the consequent small-signal can be described by

$$\frac{d}{dt}\delta \mathrm{N} = \frac{\eta_i}{qV_a}\delta \mathrm{I} - \left[\frac{1}{\tau_{\Delta N}} + \frac{v_g g_0 S_b}{1+\varepsilon S_b}\right]\delta N - \left[\frac{1}{\Gamma \tau_p} - \frac{v_g \varepsilon G S_b}{1+\varepsilon S_b}\right]\delta S, \quad (7)$$

$$\frac{d}{dt}\delta S = \frac{\Gamma v_g g_0 S_b}{1+\varepsilon S_b}\delta N - \frac{\Gamma v_g \varepsilon G S_b}{1+\varepsilon S_b}\delta S, \quad (8)$$

where $\tau_{\Delta N}$ is the differential carrier lifetime that is equal to $(A+2BN_b+3CN_b^2)^{-1}$ and the β is neglected. By manipulating Eqs. (7) and (8) to eliminate δN, a second-order system equation can be expressed as

$$\frac{d^2}{dt^2}\delta S + \gamma \frac{d}{dt}\delta S + 4\pi^2 {f_r}^2 \delta S = \frac{\eta_i}{qV_a}\frac{\Gamma v_g g_0 S_b}{1+\varepsilon S_b}\delta I, \quad (9)$$

where the resonance frequency (f_r) and the damping factor (γ) can be written by

$${f_r}^2 = \frac{1}{4\pi^2}\left[\frac{1}{\tau_p}\frac{v_g g_0 S_b}{1+\varepsilon S_b} + \frac{1}{\tau_{\Delta N}}\frac{\Gamma v_g G S_b}{1+\varepsilon S_b}\right], \quad (10)$$

$$\gamma = \frac{v_g g_0 S_b}{1+\varepsilon S_b} + \frac{\Gamma v_g g_0 S_b}{1+\varepsilon S_b} + \frac{1}{\tau_{\Delta N}}. \quad (11)$$

The modulation response can be obtained from a small sinusoidal current change as $\delta I(t) = \delta I_0 e^{j2\pi ft}$ where I_0 and f denote maximal current and time-harmonic EM field frequency, respectively. In Eq. (9), the photon density is substituted by a measurable quantity such as the optical output power (P_{out}). The optical output power can be represented by $P_{out} = \eta_0 hcSV_p/\lambda_0 \tau_p$ where

η_0, h, c, V_p, and λ_0 represent the optical efficiency, Planck constant, the speed of light, the volume of the lasing mode, and operating wavelength, respectively. To obtain an expression for the sinusoidal modulation transfer function ($H_i(f)$), the function can be written as Eq. (12) by replacing the d/dt with $j2\pi f$ in Eq. (9) and assuming $\delta S(t) = \delta S_0 e^{j2\pi ft}$ and $\delta P_{out}(t) = \delta P_0 e^{j2\pi ft}$ with S_0 and P_0 denoting maximum photon density of the lasing mode and maximum optical output power, respectively.

$$H_i(f) = \frac{\delta P_0}{\delta I_0} = \eta_d \frac{hc}{\lambda_0 q} \cdot \frac{f_r^2}{f_r^2 - f^2 + j\frac{f}{2\pi}\gamma}, \tag{12}$$

where $\eta_d = \eta_i \eta_0$ is the differential quantum efficiency. Eq. (12) is regarded as the intrinsic modulation transfer function of the VCSEL with f_r and γ. In general, the parasitic capacitance in the VCSEL and the carrier transport need to be considered for the transfer function of the signal modulation. The equivalent VCSEL circuit model of the VCSEL is assumed to discuss the effect of the parasitic capacitance and the carrier transport. Thus, the transfer function ($H_{par}(f)$) of the VCSEL can be modified as

$$H_{par}(f) = \frac{1}{1 + j\frac{f}{f_p}}, \tag{13}$$

where the f_p is the cut-off frequency. Therefore, the final transfer function can be obtained by combining the transfer functions of VCSEL and small-signal modulation. The final transfer function can be represented by

$$H(f) = H_i(f) \cdot H_{par}(f) = C \cdot \frac{f_r^2}{f_r^2 - f^2 + j\frac{f}{2\pi}\gamma} \cdot \frac{1}{1 + j\frac{f}{f_p}}. \tag{14}$$

By considering $\tau_p \ll \tau_{\Delta N}$ and $g_0 \sim \Gamma \varepsilon G$, the approximated f_r can be obtained from Eq. (10) by

$$f_r \approx \frac{1}{2\pi}\sqrt{\frac{v_g g_0 S_b}{\tau_p(1 + \varepsilon S_b)}}. \tag{15}$$

In addition, the damping factor formula can be simplified to

$$\gamma = K \cdot f_r^2 + \gamma_0 = 4\pi^2 \left[\tau_p + \frac{\varepsilon}{v_g g_0}\right] \cdot f_r^2 + \gamma_0. \tag{16}$$

where $\gamma_0 = 1/\tau_{\Delta N}$ denotes the damping factor offset. Furthermore, K indicates the K-factor. In general, the modulation bandwidth of the VCSEL is determined by three parameters in Eq. (14). Eqs. (15) and (16) can indicate the intrinsic damping limitations of the VCSEL. Owing to $f_r \propto (S_b)^{0.5}$, increasing the photon density will enhance the resonance frequency. At the same time, the damping of the system also enlarges faster to eventually limit the modulation bandwidth because of $\gamma \propto {f_r}^2 \propto S_b$. If the limiting factors of the extrinsic bandwidth are neglected, the maximal intrinsic 3-dB bandwidth of the VCSEL can be written as the function of K-factor and γ_0 by

$$f_{3dB,\max} = f_{3dB,damping} \approx \frac{2\sqrt{2}\pi}{K} - \frac{\gamma_0}{2\sqrt{2}\pi}. \tag{17}$$

However, extrinsic effects from self-heating and electrical parasitics seriously reduce the maximal modulation bandwidth to hardly reach the damping limitation [35]. According to [36], the modulation bandwidth is equal to $f_{3\,\mathrm{dB}} = 1.55 f_r$ when the damping is small ($\gamma/2\pi f \ll 1$). It indicates that the theoretical maximal 3-dB bandwidth is obtained as 1.55 times as large as the resonance frequency. Owing to the external effects of the VCSEL, the final 3-dB bandwidth will be less than the theoretical maximal 3-dB bandwidth but still higher than the resonance frequency. Therefore, it explains why the 3-dB bandwidth of the VCSEL is larger than the resonance frequency of the device.

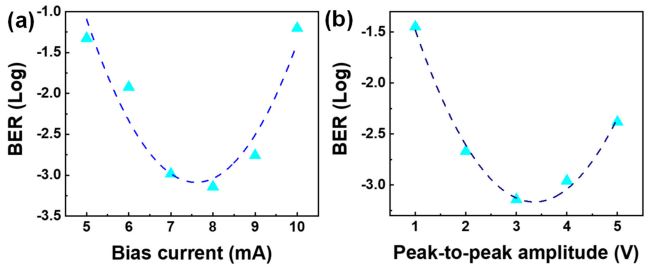

Fig. 9. The BER of the 53-Gbit/s NRZ-OOK transmission carried by the DM-VCSEL operated by different (a) bias currents and (b) V_{pp}.

B. Transmission Performance of NRZ-OOK Carried By the 5-μm DM-VCSEL

To optimize the transmission performance of the lensed OM4-MMF/100-m GI-SMF link, both the DC bias current and the V_{pp} of the data stream are respectively adjusted from 5 mA to 10 mA and from 1 V to 5 V in Fig. 9(a) and (b). Without pre-emphasizing the 53-Gbit/s NRZ-OOK waveform, the BER of the receiving data stream is decreased from 4.7×10^{-2} to 7.2×10^{-4} as the bias current increases from 5 mA to 8 mA. That is because the RIN of the DM-VCSEL is suppressed when the bias current enlarges. However, the BER is degraded to 6.2×10^{-2} when the bias current increases further to 10 mA because of the data waveform distortion induced by the output power saturation. For the V_{pp} optimization, the V_{pp} of the AWG can be adjusted. Because of the V_{pp} limitation for the AWG, the maximal output V_{pp} is only 0.8 V. Therefore, the V_{pp} of the data stream will be enlarged via a microwave amplifier with a 20-dB gain. The transmission performance with the V_{pp} optimization shows almost the same trend as the bias current optimization. The BER is decreased from 3.5×10^{-2} to 7.2×10^{-4} as the V_{pp} increases from 1 V to 3 V. Enlarging the V_{pp} to 5 V degrades the BER to 4.1×10^{-3}.

This power saturation under the high V_{pp} operation limits the transmission performance improvement. Therefore, the bias current of 8 mA and the V_{pp} of 3 V are selected as the optimal parameters for performing the transmission. The system performance improvement can be seen clearly in the eye diagrams shown in Fig. 10, where the cases of the 53-Gbit/s NRZ-OOK in the BtB and 100-m GI-SMF with and without the amplitude/phase pre-emphasis are compared. The eye diagrams of the NRZ-OOK data in both the BtB and the 100-m GI-SMF conditions without the pre-emphasis process are seriously blurred. The BER and SNR of the NRZ-OOK transmission in the BtB case are 7.4×10^{-2} and 3.2 dB, respectively. After the 100-m GI-SMF

TABLE I
THE KEY TRANSMISSION PARAMETERS OF THE 53-Gbit/s NRZ-OOK DATA CARRIED BY THE DM-VCSEL IN DIFFERENT FIBER LINKS WITH AND WITHOUT THE PRE-EMPHASIS PROCESS

Parameters	Lensed SMF	Lensed MMF	Lensed SMF+100-m GI-SMF	Lensed MMF+100-m GI-SMF
Coupling ratio (%)	9.9	100	8.4	26.1
Receving power (mW)	0.21	2.12	0.18	0.553
dP/dI (W/A)	0.033	0.342	0.028	0.088
BER	-	5.58×10^{-12}	-	6.92×10^{-10}
SNR (dB)	-	16.6	-	15.7
Peak-to-peak Jitter (ps)	-	1.301	-	1.344
Rising time (ps)	-	9.71	-	9.73
Falling time (ps)	-	9.42	-	10.35
Q Factor	-	4.9	-	4.7

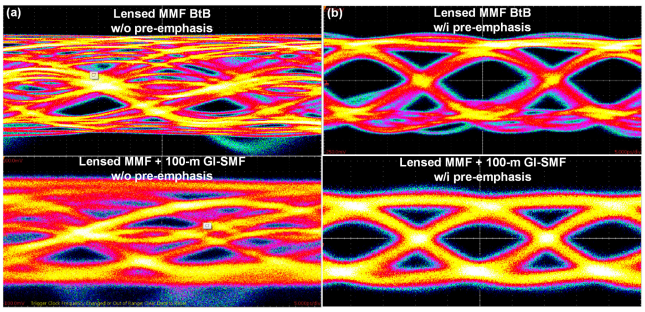

Fig. 10. Eye-diagrams of 53-Gbit/s NRZ-OOK data stream in the BtB and 100-m GI-SMF (a) without and (b) with the pre-emphasis process.

transmission, the BER and SNR are degraded to 9.8×10^{-2} and 2.2 dB, respectively.

Before implementing the pre-emphasis process, the 4-QAM OFDM data was employed to encode the DM-VCSEL. After the GI-SMF transmission, the channel response including the intensity and phase information of the entire transmission system was obtained by the received OFDM data. According to the examined channel information, the pre-emphasis with the amplitude and phase redistribution pre-compensate the degraded SNR spectra of NRZ-OOK data at the transmitting end. Therefore, the amplitude of the pre-emphasized data is reduced. This energy consumption is dependent on the deterioration of the channel response. After compensating the channel response, the 53-Gbit/s NRZ-OOK data in the 100-m GI-SMF case exhibits a better eye diagram than that without the pre-emphasis technology. That is because the pre-emphasis technology improves the whole system by sacrificing the power at the low-frequency region to compensate at the high-frequency region. The key transmission parameters of the 53 Gbit/s NRZ-OOK transmission in different fiber links are listed in Table I. For the NRZ-OOK data received by the lensed OM4-MMF, the respective SNR and BER of 16.6 dB and 5.58×10^{-12} with a corresponding peak-to-peak jitter of 1.301 ps, rising/falling times of 9.71 ps/9.42 ps, and a Q factor of 4.9 are observed. Although the coupling due to the mold field mismatch between lensed OM4-MMF and GI-SMF results in a 74% loss of optical power, the reduced number of modes results in lower chromatic dispersion. As a result, the 53-Gbit/s NRZ-OOK data stream in the 100-m GI-SMF case demonstrates better system performance with SNR of 15.7 dB and BER of 6.92×10^{-10}, peak-to-peak jitter of 1.344 ps, rising/falling times of 9.73 ps/10.35 ps, and Q factor of 4.7. For the lensed SMF case, the measured output power collected from DM-VCSEL is only 0.21 mW, lower than that of 2.12 mW received by the lensed OM4-MMF. As the coupling efficiency between lensed SMF and GI-SMF is achieved up to 85%, the final output power after the 100-m GI-SMF is only 0.18 mW, smaller than that of 0.55 mW for the lensed OM4-MMF + 100-m GI-SMF case. This power is too low to transmit the NRZ-OOK data. Therefore, the low coupling power of the lensed SMF is an important issue to be solved for the lensed SMF and GI-SMF links.

C. Transmission Performance of the 16-QAM OFDM Carried By 5 μm DM-VCSEL

To improve the data rate within the allowable bandwidth, the QAM-OFDM has also been used. The pre-emphasis method can also be used to improve the transmission result of the QAM-OFDM transmission. This method distributes the signal power to each OFDM subcarrier for compensating the SNR degradation induced by the finite channel bandwidth during transmission. Therefore, the overall modulation throughput can be improved for achieving higher data capacity within the same bandwidth. By convoluting the spectral power of the 16-QAM-OFDM data with the inverse correction transfer function of the transmission system, the power redistribution can effectively improve the degraded SNR of the data stream carried by specific OFDM subcarriers. As this transfer function of the transmission system is similar to the low-pass filter, the OFDM subcarriers at higher frequencies obtain the power compensation. Fig. 11 shows the transformed spectra, received waveforms, and decoded constellation plots of the 30 Gbit/s 16-QAM OFDM transmission with and without the pre-emphasis method. The throughput at the high-frequency region is improved with a flatter power-to-frequency slope of nearly 0 dB/GHz after the pre-emphasis process [37]. Because the spectral power in the low-frequency region is sacrificed to compensate for that in the high-frequency region, the amplitude of the waveform decreases from 156 mV to 88 mV. The EVM improves from 18.8% to 15.1% to produce a clearer constellation plot.

Note that the high peak-to-average power ratio (PAPR) of the QAM OFDM data is another important parameter to induce nonlinear distortion and waveform clipping phenomenon. In principle, the PAPR can be expressed as:

$$PAPR = \frac{\max\left\{|x_n|^2\right\}}{E\left\{|x_n|^2\right\}}, \tag{18}$$

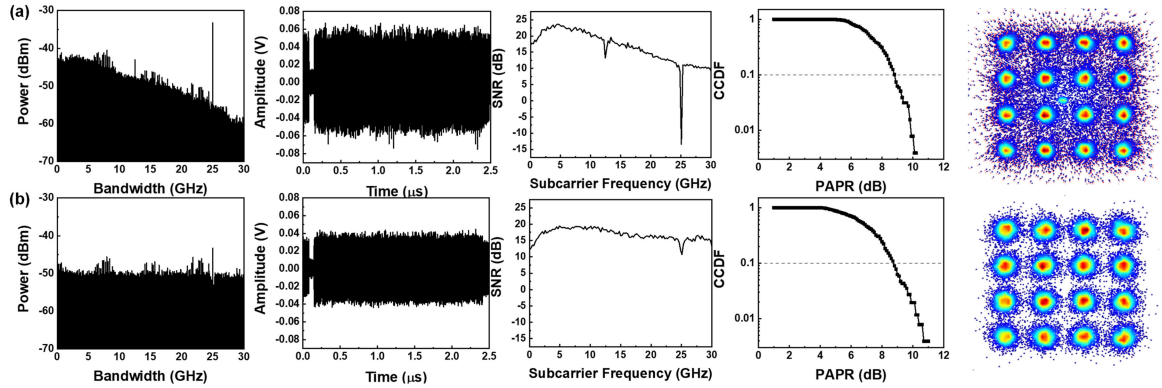

Fig. 11. Waveforms, transform spectra, PAPRs, SNRs, and constellation plots of the 30 Gbit/s 16-QAM OFDM data (a) without and (b) with the pre-emphasis.

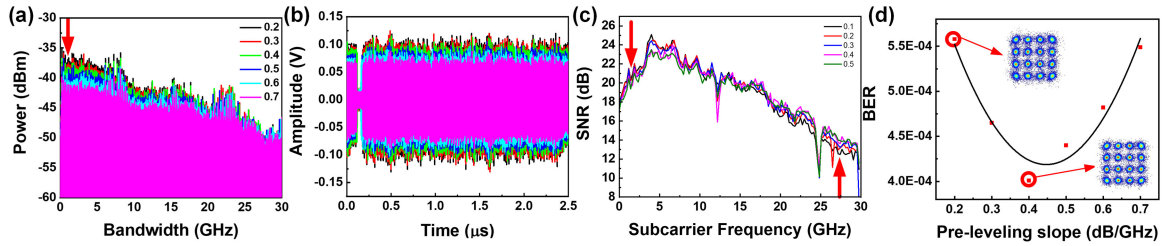

Fig. 12. The (a) transformed spectra, (b) received waveforms, (c) SNRs, (d) decoded BERs and constellation plots of the pre-leveled 16-QAM OFDM data carried by the DM-VCSEL with different pre-leveling slopes.

where x_n, $max\{\cdot\}$, and $E\{\cdot\}$, denote the time-domain waveform, the maximal value, and the expectation value, respectively. In Fig. 11, the PAPR at the complementary cumulative distribution function (CCDF) of 0.1 decreases from 8.8 dB to 8.7 dB for the QAM OFDM data with the pre-emphasis process. Moreover, the average SNR and the BER of the 30 Gbit/s 16-QAM OFDM are respectively improved from 14.5 dB to 16 dB and from 6.8×10^{-3} to 2.4×10^{-3}. Not only the pre-emphasis but also the pre-leveling methods are used to optimize the transmission performance in this work. The pre-leveling process is implemented by simply multiplying the 16-QAM OFDM spectra with a rising exponential function. Adjusting the pre-leveling power-to-frequency slope can directly compensate for the degraded power response of the OFDM subcarriers in the high-frequency region. By setting the encoding bandwidth of the 16-QAM OFDM data at 30 GHz in the BtB case, the received waveforms, transform spectra, constellation plots, SNRs, and BERs of the pre-leveled 16-QAM OFDM data by different pre-leveling slopes are shown in Fig. 12 [38]. Fig. 12(a) exhibits the power in the low-frequency region for the transform spectrum of the 16-QAM OFDM data decreases when the pre-leveling slope increases. This phenomenon also reduces the power of the waveform, as shown in Fig. 12(b). In Fig. 12(c), increasing the pre-leveling slope decreases the SNR in the low-frequency region and enhances that in the high-frequency region. To optimize the pre-leveling slope, increasing the pre-leveling slope from 0.2 to 0.4 reduces the EVM from 14.3% to 13.7% and increases the average SNR from 16.9 dB to 17.3 dB. This phenomenon also improves the BER from 5.6×10^{-4} to 4.1×10^{-4}. When the pre-leveling slope rises further to 0.7, the over-sacrificed SNR in the low-frequency region to compensate for the SNR in the high-frequency region enlarges the EVM to 13.9% and decreases the SNR to 17.4 dB. This also degrades the BER to 5.5×10^{-4}. The constellation plot of the 16-QAM OFDM data carried by the DM-VCSEL at the pre-leveling slope of 0.4 is clearer than those at the pre-leveling slopes of 0.2 and 0.7.

TABLE II
TRANSMISSION RESULTS OF THE PRE-LEVELED 16-QAM-OFDM TRANSMISSION CARRIED BY THE DM- AND SM-VCSELS IN THE BTB AND 100-m OM4-MMF CASES

Device	DM-VCSEL		SM-VCSEL	
Transimssion	BtB	100-m OM4-MMF	BtB	100-m OM4-MMF
Data Rate	136 Gbit/s	112 Gbit/s	92 Gbit/s	80 Gbit/s
SNR	16.3 dB	16.1 dB	15.5 dB	15.3 dB
BER	2.5×10^{-3}	1.7×10^{-3}	2.8×10^{-3}	3.5×10^{-3}

The comparison of the DM-VCSEL and SM-VCSEL reported in previous works is summarized in Table II [39]. Table II exhibits the transmission results of the pre-leveled 16-QAM OFDM transmission carried by the DM- and SM-VCSELs in the BtB and 100-m OM4-MMF cases. From the previous work of the SM-VCSEL modulation, the SM-VCSEL can deliver the pre-leveled 16-QAM OFDM data stream at 92 Gbit/s in the BtB case and 80 Gbit/s in the 100-m OM4 MMF case. In this work, the higher data rates of the pre-leveled 16-QAM OFDM transmission carried by the DM-VCSEL are 136 Gbit/s in the BtB case and 112 Gbit/s in the 100-m OM4 MMF case because

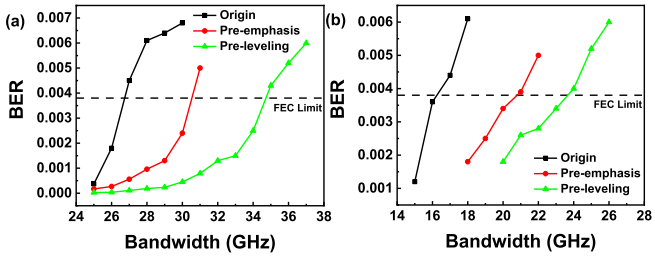

Fig. 13. BERs of the 16-QAM OFDM carried by the DM-VCSEL with different data compensation in the (a) BtB and (b) 100-m GI-SMF cases.

the DM-VCSEL exhibits larger output power than SM-VCSEL. Therefore, this DM VCSEL can be a potential candidate for the short-reached data-center application.

The maximal allowable transmission data rates of the 16-QAM OFDM carried by the DM-VCSEL are compared with different data compensation methods in the BtB and 100-m GI-SMF cases. Fig. 13(a) shows the BERs of the 16-QAM OFDM data carried by the DM-VCSEL at the different modulation bandwidths with different data compensations in the BtB case. Without any compensation, the maximal modulation bandwidth of the 16-QAM OFDM data can only reach 26 GHz with a corresponding data rate of 104 Gbit/s. This data rate is obviously smaller than 120 Gbit/s by the pre-emphasis process and 136 Gbit/s by the pre-leveling process with a slope of 0.4 dB/Hz. In addition, Fig. 13(b) also exhibits the BERs of the 16-QAM OFDM data carried by the DM-VCSEL at the different modulation bandwidths with different data compensations in the 100-m GI-SMF case. Owing to the mismatch in the optical field due to the large difference between the core diameters of OM4-MMF and GI-SMF, the high-order side modes are filtered out, which reduces the number of the transverse modes. This phenomenon also significantly reduces the output power and thus the SNR of the VCSEL. Therefore, the 100-m GI-SMF transmission without data compensation is degraded to only 64 Gbit/s. However, the data compensation can effectively improve the data rate of the 100-m GI-SMF transmission. The data rate is enhanced to 80 Gbit/s using the pre-emphasis process and further to 92 Gbit/s using the pre-leveling process with a slope of 0.4 dB/Hz. From the performance results in both the BtB and the 100-m GI-SMF transmission, the pre-leveling technology is better data compensation than others in this work.

The pre-emphasis technology analyzes the amplitude and phase components at different frequencies and calculates the weighting factors to re-distribute the total power to the OFDM subcarriers for the amplitude/phase and SNR compensation. Although this method obtains the equal SNR for all OFDM subcarriers, the high-frequency OFDM subcarriers with lower SNR needs more power to perform the amplitude/phase correction as well as the SNR compensation, which wastes lots of power for obtaining the lower average SNR of the data stream carried by the higher OFDM subcarriers. In contrast, the pre-leveling method only utilizes the simplified exponential formula to perform the data amplitude recovery without over-wasting the signal power on the phase compensation of OFDM subcarriers located beyond the -3 dB modulation bandwidth. This method slightly sacrifices less power at the lower band for compensating the throughput at the higher band. Without the excessive power consumption to perform the data pre-compensation, the pre-leveled OFDM data stream reveals a higher average SNR than the pre-emphasized OFDM data for a better receiving performance.

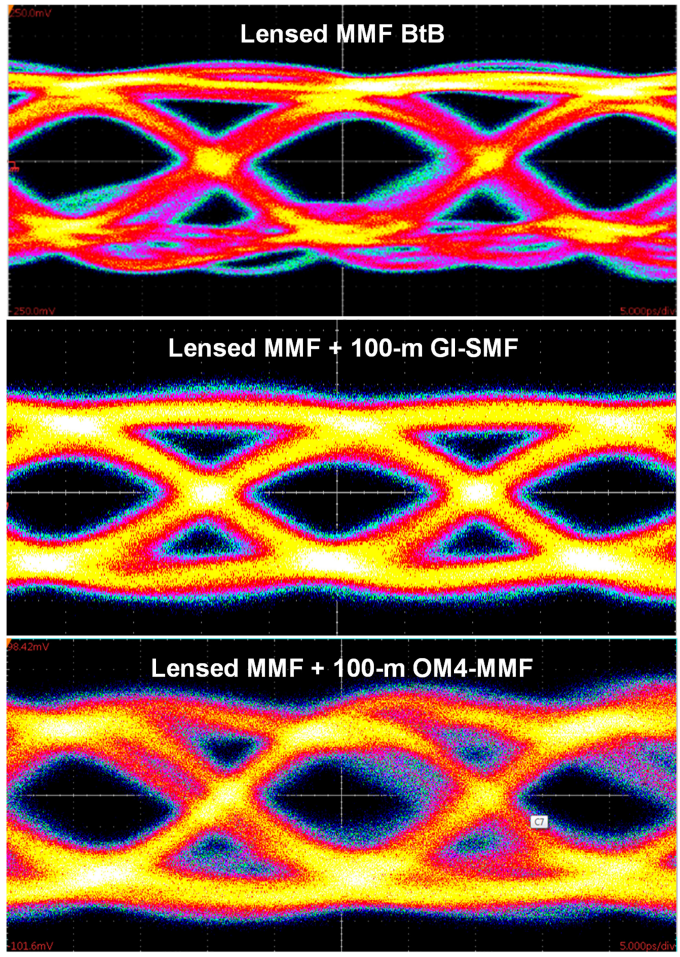

Fig. 14. Eye diagrams of the 53-Gbit/s NRZ-OOK data stream carried by DM-VCSEL in the BtB, 100-m OM4 MMF, and 100-m SMF cases.

D. Comparison of the Transmission Performance of the NRZ-OOK and QAM OFDM Data Streams in the OM4-MMF and GI-SMF Cases

Fig. 14 shows the eye diagrams of the NRZ-OOK data transmitted by the DM-VCSEL under the BtB, 100-m GI-SMF, and 100-m OM4-MMF conditions. In Fig. 14, the BER of the 53 Gbit/s NRZ-OOK carried by the DM-VCSEL after transmitting through the 100-m GI-SMF can pass the telecom standard with a BER of 10^{-9}. The corresponding BER, SNR, and Q-factor are measured as 6.9×10^{-10}, 15.7 dB, and 4.7, respectively. When the transmission medium changes from the

TABLE III
TRANSMISSION PARAMETERS OF THE 53-Gbit/s NRZ-OOK DATA STREAMS CARRIED BY THE DM-VCSEL IN THE BtB, 100-m GI-SMF, AND 100-m OM4-MMF CASES WITH THE PRE-EMPHASIS PROCESS

Parameters	BtB	100-m GI-SMF	100-m OM4-MMF
Receving power (mW)	2.12	0.55	1.91
BER	5.58×10^{-12}	6.92×10^{-10}	5.88×10^{-8}
SNR (dB)	16.6	15.7	14.5
Peak-to-peak Jitter (ps)	1.301	1.344	1.76
Rising time (ps)	9.71	9.73	9.95
Falling time (ps)	9.42	10.35	11.35
Q Factor	4.9	4.7	4.4

100-m GI-SMF to the 100-m OM4-MMF, the BER, SNR, and Q-factor deteriorate to 5.9×10^{-8}, 14.5 dB, and 4.4, respectively.

In addition, the transmission performances of the NRZ-OOK data stream in the BtB, 100-m GI-SMF, and 100-m OM4-MMF cases are also summarized and compared in Table III. The output power of the DM-VCSEL after propagating through both the 100-m GI-SMF and the 100-m OM4-MMF are obtained as 0.55 mW and 1.91 mW, respectively. For the 100-m GI-SMF propagation, the mismatch between the core diameter causes a large coupling loss between the lensed OM4-MMF and GI-SMF with a high power loss of 74%, which affects the transmission result. On the other hand, the coupling loss is much lower, only 10% for the 100-m OM4-MMF case, which slightly influences the transmission performance. However, the modal dispersion of the MMF seriously contributes to transmission deterioration. Obviously, the modal dispersion of the OM4-MMF induces large timing jitters and large rising/falling times, which degrade the SNR and the BER. The BER for the 100-m OM4-MMF case is almost two orders of magnitudes larger than that for the 100-m GI-SMF case. Therefore, both the GI-SMF and the OM4-MMF transmission have advantages such as higher coupling power for the OM4-MMF and less modal dispersion for the GI-SMF. In addition, the disadvantages including large modal dispersion for the OM4-MMF and low coupling power for the GI-SMF appear to affect the transmission performance. In general, the pulse broadening (Δt) induced by the modal dispersion can be estimated as by [40]

$$\Delta t = L\Delta\lambda\,|D|\,, \tag{19}$$

where L, $\Delta\lambda$, and D respectively denote the transmission distance, the linewidth of VCSEL, and the chromatic dispersion coefficient. In addition, the linewidth of VCSEL can also be obtained by [41]

$$\Delta\lambda = \sqrt{\left[\sum_{i=1}^{n} P_i\left(\lambda_i - \sum_{i=1}^{n} P_i\lambda_i \Big/ \sum_{i=1}^{n} P_i\right)^2\right] \Big/ \sum_{i=1}^{n} P_i}, \tag{20}$$

where P_i and λ_i respectively indicate the peak power and central wavelength of the i_{th} modes. With a special design, the GI-SMF only supports 2-3 modes as confirmed by the manufacturer. Even the MM-VCSEL output can decrease its mode number as well as linewidth after seeding into the GI-SMF. This effectively suppresses the dispersion-induced bit-shape broadening to improve the transmission performance. In future data-center applications, low modal dispersion characteristic for the GI-SMF has the potential in long-reach transmission.

Fig. 15 shows the transmission performances of the QAM OFDM data transmitted by the DM-VCSEL under the 100-m GI-SMF and 100-m OM4-MMF conditions. For an initial test shown in Fig. 15(a), the 22-Gbaud 16-QAM OFDM data after 100-m OM4-MMF propagation exhibits higher transformed spectral power and larger received waveform amplitude, as compared to those results obtained after 100-m GI-SMF propagation owing to the high coupling power of 1.91 mW for the 100-m OM4-MMF. From Fig. 15(b), the output power difference also induces the average SNRs of 16.1 dB for the 100-m OM4 MMF and 15.3 dB for the 100-m SMF. When the propagating medium changes from the 100-m OM4-MMF to the 100-m GI-SMF, the BER and EVM increase from 1.7×10^{-3} to 3.5×10^{-3} and from 15.7% to 17.2%, respectively. A cleaner constellation for the 22 Gbaud 16-QAM OFDM data after 100-m OM4-MMF propagation can also be observed in Fig. 15(c). Hence, the output power also affects the allowable data rate to pass the FEC limit. Fig. 15(d) shows that the allowable data rates after 100-m-long OM4-MMF and GI-SMF propagations reach 112 and 92 Gbit/s, respectively, because of the lower output power. For the 100-m OM4-MMF and GI-SMF cases, the error-free data rate improves to 108 and 88 Gbit/s correspondingly.

The difference in the transmission performance between the NRZ-OOK and QAM-OFDM transmission is mainly originated from the severer SNR requirement for the latter format with an advanced complex encoding algorithm. In principle, the 16-QAM-OFDM format shows a relationship between the BER and the SNR with $\mathrm{BER_{QAM}} = 0.5 \times \mathrm{erfc}\{(\mathrm{SNR}\cdot\log_2\mathrm{M})^{0.5}/[2 \times (\mathrm{M}-1)]^{0.5}\}$, requiring an error-free SNR of 22.5 dB at BER of 1×10^{-9} without employing forward error correction (FEC), whereas the SNR criterion for NRZ-OOK with a $\mathrm{BER_{NRZ\text{-}OOK}} = 0.5 \times \mathrm{erfc}[(\mathrm{SNR})^{0.5}/\sqrt{2}] = 1 \times 10^{-9}$ is only 15.6 dB. Fortunately, the error-free SNR required for the received 16-QAM-OFDM data can be further reduced to 15.2 dB for receiving with a BER $= 3.8 \times 10^{-3}$ when employing FEC. Even with FEC, a significant decay in the output power of the DM-VCSEL is observed due to the relatively small emission cross-section area, which inevitably causes a substantial drop in the SNR to degrade the transmission performance seriously. Even though the GI-SMF can reduce the modal dispersion, the low output power of the DM-VCSEL and the large coupling loss of the GI-SMF concurrently predominates in the QAM-OFDM transmission. From Fig. 15(b) and (d), the coupling power is a dominated factor affecting the transmission performances of the QAM-OFDM data. That is because the coupling power for the OM4-MMF link is four times larger than that for the GI-SMF link to seriously influence the average SNR. When the coupling power for the GI-SMF link increases to that for the OM4-MMF link, the average SNR can be enhanced to achieve better transmission performance.

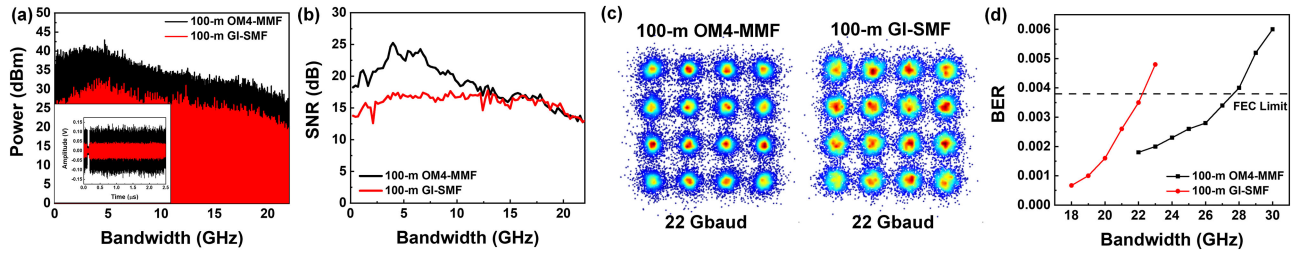

Fig. 15. The (a) transformed spectra, received waveforms, (b) SNRs, (c) constellation, and BERs of the 16-QAM OFDM data carried by DM-VCSEL in 100-m OM4 MMF and 100-m SMF cases. (d) BER of the 16-QAM OFDM data streams carried by the DM-VCSEL under different modulation bandwidths in the 100-m OM4 MMF, and 100-m SMF cases.

IV. Conclusion

In different OM4-MMF and GI-SMF links configured using lensed MMF/SMF pick-up heads and 100-m-long OM4-MMF/GI-SMF segments, the transmission performances of NRZ-OOK and 16-QAM OFDM data formats carried by the DM-VCSEL with employing different data-format pre-compensation algorithms are compared for intra-data-center applications. The employed DM-VCSEL shows a threshold current of 1.4 mA with two main transverse modes and >35-dB suppressed high-order transverse modes. Under the optimized bias current of 8 mA, the DM-VCSEL offers adequate unsaturated output power of 2.2 mW after the lensed OM4-MMF coupling. In addition, the differential resistance of the DM-VCSEL operated at 8 mA is 141 Ω to induce a reflection coefficient of 0.47, a return loss of 6.55 dB, a VSWR of 2.77, and a lower RIN of −147.5 dBc/Hz. Moreover, the core diameter mismatch between the lensed OM4-MMF and GI-SMF is used to control the mode number of the VCSEL during the transmission. After the 100-m GI-SMF transmission, the few smaller high-order transverse modes nearby the two main modes vanish to decrease the output power from 2.2 mW to 550 μW. As compared to the conventional MMF transmission, the modal dispersion is reduced in the GI-SMF transmission. Moreover, the transmission of 53 Gbit/s NRZ-OOK data carried by the DM-VCSEL with and without the pre-emphasis process in both the BtB and the 100-m GI-SMF cases is demonstrated. Without the pre-emphasis compensation, the BERs in the BtB and the 100-m GI-SMF cases are obtained as 4.6×10^{-3} and 5.1×10^{-3}, respectively. With the pre-emphasis compensation, the BER is improved to 5.6×10^{-12} for the BtB case and 6.9×10^{-10} for the 100-m GI-SMF case. For the 16-QAM OFDM transmission, the pre-leveling technology offers better data compensation than the pre-emphasis technology in BtB and the 100-m GI-SMF cases. Under the pre-leveling compensation with a pre-leveling slope of 0.4 dB/GHz, the maximal allowable data rates of the 16-QAM OFDM to pass the forward error correction are improved to 136 Gbit/s for BtB case, 112 Gbit/s for 100-m OM4-MMF case, and 92 Gbit/s for the 100-m GI-SMF case. Apparently, the limited output power of the DM-VCSEL decreases the amplitude of the received NRZ-OOK and QAM-OFDM data in the GI-SMF to affect the overall SNR. Even the modal dispersion in the GI-SMF can be reduced to improve the transmission performance. Therefore, decreasing the coupling loss from the lensed SMF by carefully designing its surface curvature as well as its numerical aperture can effectively improve the SNRs of the NRZ-OOK and QAM-OFDM data for enhancing the transmission rate.

References

[1] IEEE P802.3bs, "200 Gb/s and 400 Gb/s Ethernet Task Force," 2018. [Online]. Available: http://www.ieee802.org/3/bs/index.html
[2] D. J. Law, W. W. Diab, A. Healey, S. B. Carlson, and V. Maguire, "IEEE 802.3 Industry Connections Ethernet Bandwidth Assessment. IEEE 802.3 Ethernet Working Group," Tech. Rep., Jul. 2012. [Online]. Available: http://www.ieee802.org/3/ad_hoc/bwa/BWA_Report.pdf
[3] P. Westbergh *et al.*, "40 Gbit/s error-free operation of oxide confined 850 nm VCSEL," *Electron. Lett.*, vol. 46, no. 14, pp. 1014–1016, Jul. 2010.
[4] P. Westbergh, J. S. Gustavsson, A. Haglund, M. Sköld, A. Joel, and A. Larsson, "High speed low current density 850 nm VCSELs," *IEEE J. Sel. Topics Quantum Electron.*, vol. 15, no. 3, pp. 694–703, May/Jun. 2009.
[5] C.-H. Cheng *et al.*, "850/940-nm VCSEL for optical communication and 3D sensing," *Opto-Electron. Adv.*, vol. 1, no. 3, Apr. 2018, Art. no. 180005.
[6] Y.-H. Lin, C.-T. Tsai, W.-L. Wu, C.-H. Cheng, K.-D. Choquette, and G.-R. Lin, "Photonic crystal structured multi-mode VCSELs enabling 92-Gbit/s QAM-OFDM transmission," *J. Lightw. Technol.*, vol. 39, no. 13, pp. 4331–4340, Jul. 2021.
[7] S. A. Blokhin *et al.*, "Oxide-confined 850 nm VCSELs operating at bit rates up to 40 gbit/s," *Electron. Lett.*, vol. 45, no. 10, pp. 501–503, Jun. 2009.
[8] P. Westbergh *et al.*, "32 Gbit/s multimode fibre transmission using high-speed, low current density 850 nm VCSEL," *Electron. Lett.*, vol. 45, no. 7, pp. 366–368, Mar. 2009.
[9] H. E. Li and K. Iga, *Vertical-Cavity Surface-Emitting Laser Device.*, vol. 6, Berlin, Germany: Springer, 2003.
[10] P. Westbergh *et al.*, "High-speed 850 nm VCSELs with 28 GHz modulation bandwidth operating error-free up to 44 gbit/s," *Electron. Lett.*, vol. 48, no. 18, pp. 1145–1147, Aug. 2012.
[11] A. Gholami, D. Molin, and P. Sillard, "Compensation of chromatic dispersion by modal dispersion in MMF- and VCSEL-based gigabit ethernet transmissions," *IEEE Photon. Technol. Lett.*, vol. 21, no. 10, pp. 645–647, May 2009.
[12] R. Safaisini *et al.*, "High-speed 850 nm quasi-single-mode VCSELs for extended-reach optical interconnects," *IEEE/OSA J. Opt. Commun. Netw.*, vol. 5, no. 7, pp. 686–695, Jul. 2013.
[13] Å. Haglund, J. S. Gustavsson, J. Vukŭsić, and P. Modh, "Single fundamental-mode output power exceeding 6 mW from VCSELs with a shallow surface relief," *IEEE Photon. Technol. Lett.*, vol. 16, no. 2, pp. 368–370, Feb. 2004.
[14] K. Szczerba *et al.*, "4-PAM for high-speed short-range optical communications," *IEEE J. Opt. Commun. Netw.*, vol. 4, no. 11, pp. 885–894, Nov. 2012.
[15] R. Michalzik and K. J. Ebeling, "Generalized BV diagrams for higher order transverse modes in planar vertical-cavity laser diodes," *IEEE J. Quantum Electron.*, vol. 31, no. 8, pp. 1371–1379, Aug. 1995.
[16] M. H. MacDougal, J. Geske, C.-K. Lin, A. E. Bond, and P. D. Dapkus, "Low resistance intracavity-contacted oxide-aperture VCSELs," *IEEE Photon. Technol. Lett.*, vol. 10, no. 1, pp. 9–11, Jan. 1998.

[17] I. Harrison, H. P. Ho, B. Tuck, M. Henini, and O. H. Hughes, "Zn diffusion induced disorder in AlAs/GaAs superlatttices," *Semicond. Sci. Technol.*, vol. 4, no. 10, pp. 841–846, Oct. 1989.

[18] Y. J. Yang, T. G. Dziura, T. Bardin, S. C. Wang, and R. Fernandez, "Continuous wave single transverse mode vertical-cavity surface emitting lasers fabricated by helium implantation and zinc diffusion," *Electron. Lett.*, vol. 28, no. 3, pp. 274–276, Jan. 1992.

[19] J. W. Shi, C. C. Chen, Y. S. Wu, S. H. Guol, C. Kuo, and Y. J. Yang, "High power and high speed Zn-diffusion single fundamental mode vertical cavity surface emitting lasers at 850 nm wavelength," *IEEE Photon. Technol. Lett.*, vol. 20, no. 13, pp. 1121–1123, Jul. 2008.

[20] W. Hofmann *et al.*, "10-Gb/s data transmission using BCB passivated 1.55 μm InGaAlAs-InP VCSELs," *IEEE Photon. Technol. Lett.*, vol. 18, no. 2, pp. 424–426, Jan. 2006.

[21] K. Li, X. Chen, J. E. Hurley, J. S. Stone, and M. Li, "High data rate few-mode transmission over graded-index single-mode fiber using 850 nm single-mode VCSEL," *Opt. Exp.*, vol. 27, pp. 21395–21404, 2019.

[22] D. M. Kuchta *et al.*, "A 71-Gb/s NRZ modulated 850-nm VCSEL-based optical link," *IEEE Photon. Technol. Lett.*, vol. 27, no. 6, pp. 577–580, Mar. 2015.

[23] K. Szczerba, P. Westbergh, E. Agrell, M. Karlsson, P. A. Andrekson, and A. Larsson, "Comparison of intersymbol interference power penalties for OOK and 4-PAM in short-range optical links," *J. Lightw. Technol.*, vol. 31, no. 22, pp. 3525–3534, Nov. 2013.

[24] F. Karinou, L. Deng, R. R. Lopez, K. Prince, J. B. Jensen, and I. T. Monroy, "Performance comparison of 850-nm and 1550-nm VCSELs exploiting OOK, OFDM, and 4-PAM over SMF/MMF links for low-cost optical interconnects," *Opt. Fiber Technol.*, vol. 19, no. 3, pp. 206–212, Jun. 2013.

[25] H.-Y. Kao *et al.*, "Few-mode VCSEL chip for 100-Gb/s transmission over 100 m multimode fiber," *Photon. Res.*, vol. 5, no. 5, pp. 507–515, 2017.

[26] I.-C. Lu *et al.*, "Very high bit-rate distance product using high-power single-mode 850-nm VCSEL with discrete multitone modulation formats through OM4 multimode fiber," *IEEE J. Sel. Topics Quantum Electron.*, vol. 21, no. 6, pp. 444–452, Nov. 2015.

[27] R. Puerta *et al.*, "107.5 Gb/s 850 nm multi- and single-mode VCSEL transmission over 10 and 100 m of multi-mode fiber," in *Proc. Opt. Fiber Commun. Conf.*, 2016, Paper Th5B.5.

[28] L. A. Coldren, S. W. Corzine, and M. L. Mašanović, *Diode Lasers and Photonic Integrated Circuits*. 2nd ed., Hoboken, NJ, USA: Wiley, 2012.

[29] W. D. Laidig *et al.*, "Disorder of an alas-gaas superlattice by impurity diffusion," *Appl. Phys. Lett.*, vol. 38, no. 10, pp. 776–778, May 1981.

[30] N. H. Ky *et al.*, "Self-interstitial mechanism for zn diffusion-induced disordering of $GaAs/Al_xGa_{1-x}As$ (x = 0.1-1) multiple-quantum-well structures," *J. Appl. Phys.*, vol. 73, no. 8, pp. 3769–3781, Apr. 1993.

[31] K. Li, X. Chen, J. E. Hurley, J. Stone, and M.-J. Li, "Modal delay and modal bandwidth measurements of bi-modal optical fibers through a frequency domain method," *Opt. Fiber Technol.*, vol. 55, Mar. 2020, Art. no. 102145.

[32] P. P. Baveja *et al.*, "Assessment of VCSEL thermal rollover mechanisms from measurements and empirical modeling," *Opt. Exp.*, vol. 19, no. 16, pp. 15490–15505, Aug. 2011.

[33] W.-C. Lo *et al.*, "Effect of chirped dispersion and modal partition noise on multimode VCSEL encoded with NRZ-OOK and PAM-4 formats," *IEEE J. Sel. Topics Quantum Electron.*, vol. 28, no. 1, Jan./Feb. 2022, Art. no. 1500409.

[34] H.-Y. Wang, C.-H. Cheng, and G.-R. Lin, "P suppression of relative intensity and mode partition noises in orthogonally polarized dual-wavelength VCSEL," *J. Lightw. Technol.*, vol. 38, no. 23, pp. 6612–6622, Dec. 2021.

[35] S. E. Hashemi, "Relative intensity noise (RIN) in high-speed VCSELs for short reach communication," M.S. thesis, Dept. Microtechnol. Nanosci., Chalmers Univ., Göteborg, Sweden, 2012.

[36] M. H. Mao, T. Y. Wu, D. C. Wu, F. Y. Chang, and H. H. Lin, "Relaxation oscillations and damping factors of 1.3 μm in (Ga) As/GaAs quantum-dot lasers," *Opt. Quantum Electron.*, vol. 36, pp. 927–933, Aug. 2004.

[37] Y.-H. Lin *et al.*, "100-Gbit/s/λ EML transmitter and PIN-PD+TIA receiver-based inter-data center link," *IEEE/OSA J. Lightw. Technol.*, vol. 38, no. 8, pp. 2144–2151, Apr. 2020.

[38] C.-Y. Huang *et al.*, "Comparison of high-speed PAM4 and QAM-OFDM data transmission using single-mode VCSEL in OM5 and OM4 MMF links," *IEEE J. Sel. Top. Quantum Electron.*, vol. 26, no. 4, Jul./Aug. 2020, Art. no. 1500210.

[39] H.-Y. Kao *et al.*, "Comparison of single-/few-/multi-mode 850 nm VCSELs for optical OFDM transmission," *Opt. Exp.*, vol. 25, no. 14, pp. 16347–16363, Jul. 2017.

[40] G. Stepniak, M. Schüppert, and C.-A. Bunge, "8 - Polymer-optical fibres for data transmission," in *Polymer Optical Fibres- Fibre Types, Materials, Fabrication, Characterisation and Applications*, C.-A. Bunge, T. Gries, and M. Beckers, Eds. Amsterdam, Netherlands: Elsevier, 2017, pp. 217–310.

[41] P. Westbergh, J. S. Gustavsson, Å. Haglund, M. Sköld, A. Joel, and A. Larsson, "High speed low current density 850 nm VCSELs," *IEEE J. Sel. Topics Quantum Electron.*, vol. 15, no. 3, pp. 694–703, May/Jun. 2009.